Electronic temperatures of terahertz quantum cascade active regions with phonon scattering assisted injection and extraction scheme

Pietro Patimisco,[1] Gaetano Scamarcio,[1,*] Maria Vittoria Santacroce,[1] Vincenzo Spagnolo,[1] Miriam Serena Vitiello,[2,3] Emmanuel Dupont,[4] Sylvain R. Laframboise,[4] Saeed Fathololoumi,[4] Ghasem S. Razavipour,[5] and Zbigniew Wasilewski[4,5]

[1]*Dipartimento Interateneo di Fisica, Università degli studi di Bari "Aldo Moro" and Politecnico di Bari, and CNR-Istituto di Fotonica e Nanotecnologie, UOS Bari, Via Amendola 173, 70126 Bari, Italy*

[2]*NEST, Istituto Nanoscienze–CNR and Scuola Normale Superiore, Piazza San Silvestro 12, Pisa I-56127, Italy*

[3]*CNR – Dipartimento di Scienze Fisiche e Tecnologie della Materia, Largo E. Fermi 5, 50125 Firenze, Italy*

[4]*National Research Council of Canada, Ottawa, Ontario, Canada*

[5]*Department of Electrical and Computer Engineering, Waterloo Institute for Nanotechnology, University of Waterloo, Canada*

[*]*gaetano.scamarcio@uniba.it*

Abstract: We measured the lattice and subband electronic temperatures of terahertz quantum cascade devices based on the optical phonon-scattering assisted active region scheme. While the electronic temperature of the injector state (j = 4) significantly increases by $\Delta T = T_e^4 - T_L$ ~40 K, in analogy with the reported values in resonant phonon scheme (ΔT ~70-110 K), both the laser levels (j = 2,3) remain much colder with respect to the latter (by a factor of 3-5) and share the same electronic temperature of the ground level (j = 1). The electronic population ratio n_2/n_1 shows that the optical phonon scattering efficiently depopulates the lower laser level (j = 2) up to an electronic temperature T_e ~180 K.

©2013 Optical Society of America

OCIS codes: (140.5965) Semiconductor lasers, quantum cascade; (250.5230) Photoluminescence.

References and links

1. R. Köhler, A. Tredicucci, F. Beltram, H. E. Beere, E. H. Linfield, A. G. Davies, D. A. Ritchie, R. C. Iotti, and F. Rossi, "Terahertz semiconductor-heterostructure laser," Nature **417**(6885), 156–159 (2002).
2. B. S. Williams, S. Kumar, Q. Hu, and J. L. Reno, "High-power terahertz quantum-cascade lasers," Electron. Lett. **42**(2), 89–91 (2006).
3. M. S. Vitiello, G. Scamarcio, V. Spagnolo, S. S. Dhillon, and C. Sirtori, "Terahertz quantum cascade lasers with large wall-plug efficiency," Appl. Phys. Lett. **90**(19), 191115 (2007).
4. M. I. Amanti, M. Fischer, G. Scalari, M. Beck, and J. Faist "Low-divergence single-mode terahertz quantum cascade laser," Nat. Photonics **3**(10), 586–590 (2009).
5. M. S. Vitiello, L. Consolino, S. Bartalini, A. Taschin, A. Tredicucci, M. Inguscio, and P. De Natale, "Quantum-limited frequency fluctuations in a terahertz laser," Nat. Photonics **6**(8), 525–528 (2012).
6. J. Xu, J. M. Hensley, D. B. Fenner, R. P. Green, L. Mahler, A. Tredicucci, M. G. Allen, F. Beltram, H. E. Beere, and D. A. Ritchie, "Tunable terahertz quantum cascade lasers with an external cavity," Appl. Phys. Lett. **91**(12), 121104 (2007).
7. S. Kumar, C. W. I. Chan, Q. Hu, and J. L. Reno, "A 1.8-THz quantum cascade laser operating significantly above the temperature of $\hbar\omega/k_B$," Nat. Phys. **7**(2), 166–171 (2011).
8. S. Fathololoumi, E. Dupont, C. W. I. Chan, Z. R. Wasilewski, S. R. Laframboise, D. Ban, A. Mátyás, C. Jirauschek, Q. Hu, and H. C. Liu, "Terahertz quantum cascade lasers operating up to ~200 K with optimized oscillator strength and improved injection tunneling," Opt. Express **20**(4), 3866–3876 (2012).
9. E. Dupont, S. Fathololoumi, Z. R. Wasilewski, G. Aers, S. R. Laframboise, M. Lindskog, S. G. Razavipour, A. Wacker, D. Ban, and H. C. Liu, "A phonon scattering assisted injection and extraction based terahertz quantum cascade laser," J. Appl. Phys. **111**(7), 073111 (2012).

#185600 - $15.00 USD Received 19 Feb 2013; revised 22 Mar 2013; accepted 22 Mar 2013; published 16 Apr 2013

10. K. Fujita, M. Yamanishi, S. Furuta, K. Tanaka, T. Edamura, T. Kubis, and G. Klimeck, "Indirectly pumped 3.7 THz InGaAs/InAlAs quantum-cascade lasers grown by metal-organic vapor-phase epitaxy," Opt. Express **20**(18), 20647–20658 (2012).
11. S. G. Razavipour, E. Dupont, S. Fathololoumi, C. W. I. Chan, M. Lindskog, Z. R. Wasilewski, G. Aers, S. R. Laframboise, A. Wacker, Q. Hu, D. Ban, and H. C. Liu (unpublished).
12. R. Nelander and A. Wacker, "Temperature dependence of the gain profile for terahertz quantum cascade lasers," Appl. Phys. Lett. **92**(8), 081102 (2008).
13. M. S. Vitiello, G. Scamarcio, V. Spagnolo, B. S. Williams, S. Kumar, Q. Hu, and J. L. Reno, "Measurement of subband electronic temperatures and population inversion in THz quantum-cascade lasers," Appl. Phys. Lett. **86**(11), 111115 (2005).
14. M. S. Vitiello, G. Scamarcio, V. Spagnolo, J. Alton, S. Barbieri, C. Worrall, H. E. Beere, D. A. Ritchie, and C. Sirtori, "Thermal properties of THz quantum cascade lasers based on different optical waveguide configurations," Appl. Phys. Lett. **89**(2), 021111 (2006).
15. M. S. Vitiello, G. Scamarcio, V. Spagnolo, T. Losco, R. P. Green, A. Tredicucci, H. E. Beere, and D. A. Ritchie, "Electron-lattice coupling in bound-to-continuum THz quantum-cascade lasers," Appl. Phys. Lett. **88**(24), 241109 (2006).
16. S. Fathololoumi, E. Dupont, S. G. Razavipour, S. R. Laframboise, G. Parent, Z. Wasilewski, H. C. Liu, and D. Ban, "On metal contacts of terahertz quantum cascade lasers with a metal–metal waveguide," Semicond. Sci. Technol. **26**(10), 105021 (2011).
17. V. Spagnolo, M. Troccoli, G. Scamarcio, C. Becker, G. Glastre, and C. Sirtori, "Thermal resistance and temperature characteristics of GaAs/Al0.33Ga0.67As quantum cascade lasers," Appl. Phys. Lett. **78**(9), 1177–1179 (2001).
18. V. Spagnolo, G. Scamarcio, H. Page, and C. Sirtori, "Simultaneous measurement of the electronic and lattice temperatures in $GaAs/Al_{0.45}Ga_{0.55}As$ quantum-cascade lasers: Influence on the optical performance," Appl. Phys. Lett. **84**(18), 3690 (2004).
19. M. S. Vitiello, G. Scamarcio, V. Spagnolo, C. Worrall, H. E. Beere, D. A. Ritchie, C. Sirtori, J. Alton, and S. Barbieri, "Subband electronic temperatures and electron-lattice energy relaxation in terahertz quantum cascade lasers with different conduction band offsets," Appl. Phys. Lett. **89**(13), 131114 (2006).
20. G. Scamarcio, M. S. Vitiello, V. Spagnolo, S. Kumar, B. Williams, and Q. Hu, "Nanoscale heat transfer in quantum cascade lasers," Physica E **40**(6), 1780–1784 (2008).
21. J. Shah, *Hot Carriers in Semiconductor Nanostructures: Physics and Applications* (Academic, 1992).
22. J. A. Gardecki and M. Maroncelli, "Set of secondary emission standards for calibration of the spectral responsivity in emission spectroscopy," Appl. Spectrosc. **52**(9), 1179–1189 (1998).
23. V. Spagnolo, G. Scamarcio, D. Marano, M. Troccoli, F. Capasso, C. Gmachl, A. M. Sergent, A. L. Hutchinson, D. L. Sivco, A. Y. Cho, H. Page, C. Becker, and C. Sirtori, "Thermal characteristics of quantum-cascade lasers by micro-probe optical spectroscopy," IEE Proc., Optoelectron. **150**(4), 298–305 (2003).
24. J. Martinez-Pastor, A. Vinattieri, L. Carraresi, M. Colocci, P. Roussignol, and G. Weimann, "Temperature dependence of exciton lifetimes in $GaAs/Al_xG_{1-x}As$ single quantum wells," Phys. Rev. B **47**(16), 10456–10460 (1993).
25. M. S. Vitiello, G. Scamarcio, and V. Spagnolo, "Temperature dependence of thermal conductivity and boundary resistance in thz quantum cascade lasers," IEEE, J. Select. Topics in Quant. Electron. **14**, 431–435 (2008).
26. M. S. Vitiello, G. Scamarcio, J. Faist, G. Scalari, C. Walther, E. H. Beere, and D. A. Ritchie, "Probing quantum efficiency by laser-induced hot-electron cooling," Appl. Phys. Lett. **94**(2), 021115 (2009).

1. Introduction

Terahertz quantum cascade lasers (QCLs) are the most promising solid state terahertz sources [1]. Significant performance improvement in terms of power [2], wall-plug efficiency [3], beam quality [4], linewidth [5] and wavelength tunability [6] have been reported. However, their temperature performance, so far limited to heat sink temperatures T_H < 200 K [7,8], is still a key issue. Active regions based on the resonant tunneling scheme for the population of the upper laser level have so far shown a maximum operating temperature $T_H \sim \hbar\omega/K_B$ [7], where K_B is the Boltzmann constant. For instance, the maximum operating temperature (~200 K) of the device reported in [8] is about 1.28 $\hbar\omega/K_B$. Designing the energy separation between the lower laser level and the ground state subband resonant to the LO-phonon energy (E_{LO}) is very effective for the fast depopulation of the lower laser level (the so-called resonant phonon scheme). On the other hand, the use of scattering-assisted (SA) injection schemes, in which the energy difference between the injector state and the upper laser level is also close to E_{LO}, is very promising for the attainment of terahertz laser action at T_H > 200 K [7,9,10]. Recently, THz QCL devices based on phonon-SA active region scheme have been realized,

#185600 - $15.00 USD Received 19 Feb 2013; revised 22 Mar 2013; accepted 22 Mar 2013; published 16 Apr 2013
(C) 2013 OSA

showing lasing at 2.4 THz up to 152 K (~1.3 $\hbar\omega/K_B$) in pulsed operation [11] and at 1.8 THz to 163 K (~1.9 $\hbar\omega/K_B$) [7].

A critical understanding of the actual lattice temperature (T_L) and the nature of the electronic distribution and particularly the individual j-th subband electronic temperatures (T_e^j) is crucial to validate theoretical models and to refine the design of THz QCL active regions with improved thermal performance [10]. The temperature dependence of the physical parameters controlling the laser rate equations, i.e. intersubband transitions rates, the Debye screening length [12] and the existence of hot-electron distributions have been neglected so far. Thermalized subband electron distributions characterized by the same electronic temperature in all subbands [9] are typically assumed in theoretical models. However, microprobe band-to-band photoluminescence spectroscopy experiments demonstrated that in THz QCLs $T_e^j > T_L > T_H$ [13–15]. In addition, the combination of a resonant-tunneling injection and a resonant-phonon depopulation scheme, causes a strong increase of the upper laser level temperature by ΔT ~100 K [13], while the ground-state temperature remains almost close to the lattice one.

In this work, we have compared the lattice temperatures and the subband electronic temperatures, in three $GaAs/Al_{0.25}Ga_{0.75}As$ active regions structures based on the phonon scattering both for the population of the upper laser level and the depletion of the lower laser one. A hot electron distribution has been found in all investigated cases. However, a maximum electron heating T_e^j -T_L ~40 K, much lower than the typical value reported for the QCLs based on the resonant phonon transitions only for the depopulation of the lower laser level, has been found.

2. Investigated samples

Three active region designs based on the phonon SA injection scheme have been investigated. Figure 1 shows the conduction and valence band structures of the three samples, while in Table 1 are reported the squared moduli of the overlap integrals $|\langle\psi_j|\psi_k\rangle|^2$ between conduction (j) and valence (k) subband envelope functions.

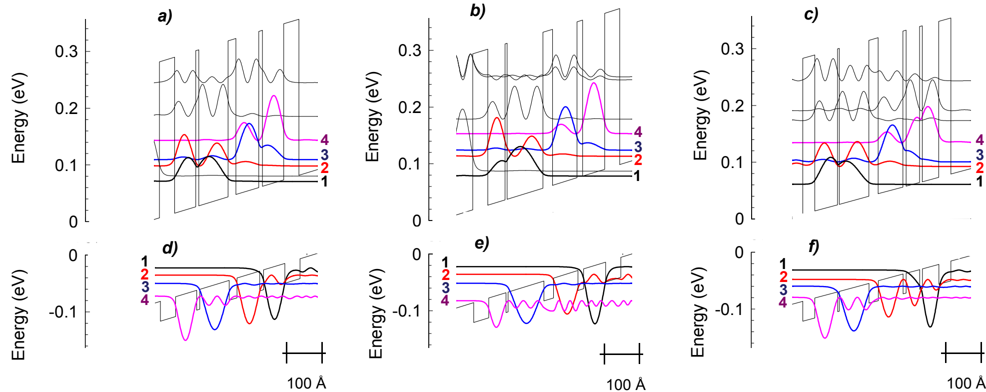

Fig. 1. Calculated conduction (a-c) and valence (d-f) band structures (1 period) of the investigated $GaAs/Al_{0.25}Ga_{0.75}As$ samples *a* (V0843), *b* (V0845) and *c* (V0962) under applied voltages per period / electric field of (67.1 mV / 18.6 kV/cm), (71.8 mV / 18.7 kV/cm), and (64.5 mV / 16.4 kV/cm), respectively. A 75% conduction-band offset, corresponding to a 0.275 eV barrier height, was used. Starting from the injection barrier, the layers thickness in (Å) are (from right to left) (a): **<u>44</u>**/63/**11**/67/**23**/85/**9**/61, (b) **44**/<u>64</u>/**16**/72/**28**/104/**6**/50, and (c) **35**/<u>48</u>/**8**/39/**9**/72/**27**/86/**5**/66. The total number of periods are 276, 260 and 253 for samples *(a)*, *(b)*, and *(c)*. The barriers are indicated in bold fonts. The underlined layers are doped. Samples *(a)* and *(b)* are center delta-doped with Si to a sheet density of $n = 3.25 \cdot 10^{10}$ cm^{-2} and $n = 3.46 \cdot 10^{10}$ cm^{-2}, respectively. Sample *(c)* is conventionally doped to $n = 1.5 \cdot 10^{17}$ cm^{-3} in the center 2 nm of the 4.8 nm quantum well.

#185600 - $15.00 USD Received 19 Feb 2013; revised 22 Mar 2013; accepted 22 Mar 2013; published 16 Apr 2013
(C) 2013 OSA

The laser emission frequencies measured at 10 K and close to threshold for QCLs having the same structures of sample (a), (b), and (c) are 2.8 THz, 2.4 THz, 2.45 THz and the maximum operating temperatures reached in pulsed mode are 138 K [9], 128.5 K, 144 K, respectively.

Table 1. The squared moduli of the overlap integrals $|\langle\psi j|\psi k\rangle|^2$ between conduction (j) and valence (k) subband envelope functions are reported from top to bottom for sample *(a)*, *(b)* and *(c)*, respectively. This calculation is performed at the electric field values of Fig. 1. Bold values marks the transitions $j \rightarrow k$ with $|\langle\psi j|\psi k\rangle|^2 \gtrsim 0.2$.

(a)

k \ j	1	2	3	4
1	2.9E-04	0.027	**0.478**	**0.529**
2	0.007	0.109	**0.293**	**0.200**
3	**0.506**	**0.251**	0.064	2.7E-03
4	**0.250**	0.158	0.009	7.7E-04

(b)

k \ j	1	2	3	4
1	3.8E-05	0.008	**0.192**	**0.697**
2	0.002	0.068	**0.615**	**0.188**
3	**0.524**	0.165	0.016	0.001
4	**0.244**	0.150	0.004	0.003

(c)

k \ j	1	2	3	4
1	3.4E-05	0.010	0.072	**0.534**
2	0.001	0.099	**0.428**	0.001
3	**0.316**	**0.285**	0.080	0.002
4	**0.299**	0.156	0.049	0.001

The main difference between the three structures is in the energies of the phonon-assisted transitions 4⟶3 and 2⟶1 (see Table 2) as compared with the LO phonon energy E_{LO} = 36 meV.

Table 2. Energies of relevant intersubband transitions of Fig. 1. E_{43} corresponds to the phonon scattering assisted injection; E_{32} is the laser transition energy; E_{21} is associated with the depletion of the lower laser level.

	Sample *(a)*	Sample *(b)*	Sample *(c)*
E_{43} (meV)	34.4	30.1	35.4
E_{32} (meV)	10.3	9.5	7.4
E_{21} (meV)	29.5	34.3	34.4

A PdGeTiPtAu metallization process was used to fabricate top and bottom alloyed Ohmic contacts and In-Au wafer bonding technique was applied to transfer the epi-layers to a host

#185600 - $15.00 USD Received 19 Feb 2013; revised 22 Mar 2013; accepted 22 Mar 2013; published 16 Apr 2013
(C) 2013 OSA

GaAs n^+. Mesa devices were fabricated by reactive-ion etching [16]. Electrical contacts are obtained by gold wire-bonding directly onto the top of the devices. The areas of devices *(a), (b)*, and *(c)* are A = 70 µm × 170 µm, A = 75 µm × 170 µm, and A = 145 µm × 180 µm, respectively. The thickness of the active region is d = 10 µm for all samples.

Figure 2 shows the voltage drop per stage (V) measured in continuous wave (CW) at T_H = 50 K as a function of the current density (J). A first resonance, corresponding to 1'-3 (sample *(a)*) and 1'-2 (sample *(b)* and *(c)*) level alignment, can be observed at ~9 mV, ~25 mV, and ~17 mV, in sample *(a)*, *(b)* and *(c)*, respectively. At larger voltages, a negative differential resistance (NDR) region is evident in the range (27 mV - 60 mV), (30 mV - 65 mV), and (25 mV - 60 mV), in sample *(a)*,*(b)* and *(c)* respectively. The flat monotonic increase of J at V > 64 mV, V > 67 mV, and V > 62 mV, in sample *(a)*,*(b)*, and *(c)*, corresponds to the band alignment for tunnel injection into level 4, in good agreement with the calculations shown in Fig. 1.

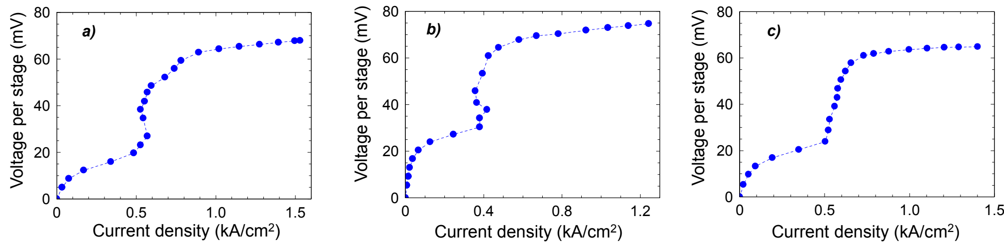

Fig. 2. (a-c): the current density (J)-voltage per stage (V) characteristics of sample a, b, and c in continuous-wave (CW) operation and at the heat sink temperature TH = 50 K. Dashed lines are guides for eyes.

3. Experimental setup

The lattice and electronic temperatures were extracted by analyzing microprobe band-to-band photoluminescence (PL) spectra, as a function of continuous current density and bias voltage. This technique has already proved successful for the investigation of mid-IR [17, 18] and THz [13–15, 19, 20] QCLs. The PL signal was obtained by focusing the 647-nm line of a Kr^+ laser directly onto the QCL front facet in an Airy disk of about ~2 µm diameter, by using an 80X long working distance achromatic microscope objective lens. The devices were mounted into a helium-flow micro-cryostat including a 0.5 mm quartz window. We simultaneously measured the temperature of the heat sink and device copper mount, by using a thermocouple and a calibrated Si-diode, respectively. In our experiment the copper mount temperature was kept at the constant value of T_H = 50 K. The incident power density was kept below ~500 W/cm^2, that caused a local laser-induced heating < 6 K. The estimated density of photogenerated carriers in the device is in the range 0.5-1 × 10^{15} cm^{-3}, 1-2 orders of magnitude lower than the doping level in the active region. The laser excitation mostly provides the valence band holes needed to probe the electronic population via band-to-band radiative recombination.

The PL signal was transmitted through an holographic notch filter, dispersed using a 0.64 m monochromator equipped with a 600 lines/mm grating and detected with a Si charge coupled device cooled to 134 K. A spectral resolution of 0.2 meV is used. All experimental spectra were recorded by focusing the Kr^+ laser spot on the cleaved side facet of the mesas, in the middle of the active region.

Preliminarily to the spectral analysis, the PL spectra have been corrected for the spectral response of the spectroscopic setup. The typical approach to determine the experimental response function is based on calibration procedure using radiation sources whose emission spectral lineshape are known, e.g. black body-like emitters. We have used as an internal standard the high energy portion of the luminescence spectra emitted from the thermalized

#185600 - $15.00 USD Received 19 Feb 2013; revised 22 Mar 2013; accepted 22 Mar 2013; published 16 Apr 2013
(C) 2013 OSA

two-dimensional electron gas of the investigated samples, without applied voltage. In fact, the corresponding lineshape is characterized by a simple exponential decay at increasing photon energy [21]. Our approach has the advantage of inherently taking into account geometrical effect corrections that otherwise affect the calibrations based on the comparison with a standard light source [22].

4. Lattice and electronic temperatures

Figure 3 shows a set of representative PL spectra recorded in the temperature range $T_L = T_H$ = 50 K - 300 K with no applied voltage for sample *(c)*. The main peak energy (E_{11}), ascribed to the transition between the ground conduction and valence subbands (see Figs. 1(c), 1(f)), redshifts with temperature following the monotonic trend shown in the inset of Fig. 3. Similar trends are observed in all investigated samples and can be used as temperature calibration curves. If a voltage is applied to the devices the local lattice temperature increases due to the dissipated electrical power is readily obtained with a resolution of ~0.5 K from the red shift ΔE_{13} of the main PL peak (see later), assuming that the energy of the transition 1→3 has a temperature dependence identical to the 1→1 transition [23]. When the device is off the electronic temperatures extracted from the high energy exponential slope of the PL spectra corresponds to the lattice one.

If a voltage is applied, the high energy conduction subbands start to be aligned and populated. The radiative recombination between populated conduction subbands and photogenerated holes gives origin to additional structure on the high energy side of the PL spectra, whose intensity is well reproduced by the following expression:

$$I_{PL}(E) \propto \sum_{j=1}^{4}\sum_{k=1}^{4} A_{jk} E_{jk}{}^{4} \left|\psi_j | \psi_k\right|^2 \mathcal{L}(E) \qquad (1)$$

where $A_{jk} = n_j \cdot p_k$; n_j and p_k are the populations of the conduction and valence subband. The lineshape function $\mathcal{L}$(E) is obtained joining a Lorentzian with a phenomenological broadening $\Gamma(T_L)$ on the low energy side and an exponential decay on the high energy side of the main peak, respectively:

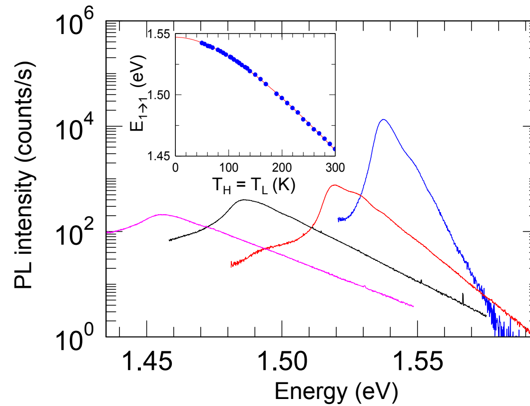

Fig. 3. Representative photoluminescence spectra of sample (c) at lattice temperatures of 50 K, 130 K, 220 K and 300 K without any applied voltage. The corresponding integration times are: 1 s, 25 s, 80 s, and 180 s. The high energy slope of each curve depends exponentially on the electronic temperature as described in the text. Inset: Temperature dependence of peak energy $E_{1\to1}$. The solid line is the best fit obtained using a Varshni-like function $E_{11}(T_L) = E_{11}(0) - \frac{\alpha T_L^2}{\beta + T_L}$ with $E_{11}(0)$ = 1.547 eV, $\alpha = 5.93 \times 10^{-4}$ eV/K^2 and β = 277 K.

#185600 - $15.00 USD Received 19 Feb 2013; revised 22 Mar 2013; accepted 22 Mar 2013; published 16 Apr 2013
(C) 2013 OSA

$$\mathcal{L}(E) = \begin{cases} \dfrac{A}{2\pi} \dfrac{\Gamma(T_L)}{(E - E_{jk})^2 + \Gamma^2(T_L)} & E < E_{jk} + \Delta_j \\ Be^{-E\left(\frac{1}{K_B T_e^j} + \frac{m_e^*}{m_{hh}^*} \frac{1}{K_B T_{hh}}\right)} & E > E_{jk} + \Delta_j \end{cases} \quad (2)$$

where T_e^j, T_{hh} are the electron subband and heavy-hole temperatures, $m_e^* = 0.067$ and $m_{hh}^* = 0.51$ are the electron and heavy-hole effective masses, E_{jk} is the j→k transition energy. The ratio A/B and Δ_j must been chosen to ensure the continuity between the two portions of. $\mathcal{L}$ It is well accepted that the heavy hole temperature is close to the lattice one under moderate to high electric fields [21] so that we assume $T_{hh} = T_L$. For the temperature dependence of the linewidth $\Gamma(T_L)$ we used:

$$\Gamma(T_L) = \Gamma_0 + aT_L + \frac{b}{e^{\frac{\hbar\omega_{LO}}{K_B T_L}} - 1} \quad (3)$$

where $\Gamma_0 = 1.66$ meV, $a = 11.6 \times 10^{-3}$ meV/K and $b = 15.6$ meV [24].

An excellent reproduction of the photoluminescence spectra recorded under applied voltage was obtained by using Eqs. (1)–(3), considering the j→k transitions having an overlap integral $\gtrsim$ 0.2 (see the Table 2) and leaving only E_{13}, T_e^j and A_{jk} as fitting parameters. The (E_{jk} - E_{13}) energy differences are extracted from band structure calculations assuming temperature independence of the intersubband transitions. Figure 4 shows representative PL spectra and best fit curves for samples (*a-c*) corresponding to the band alignments of Fig. 1.

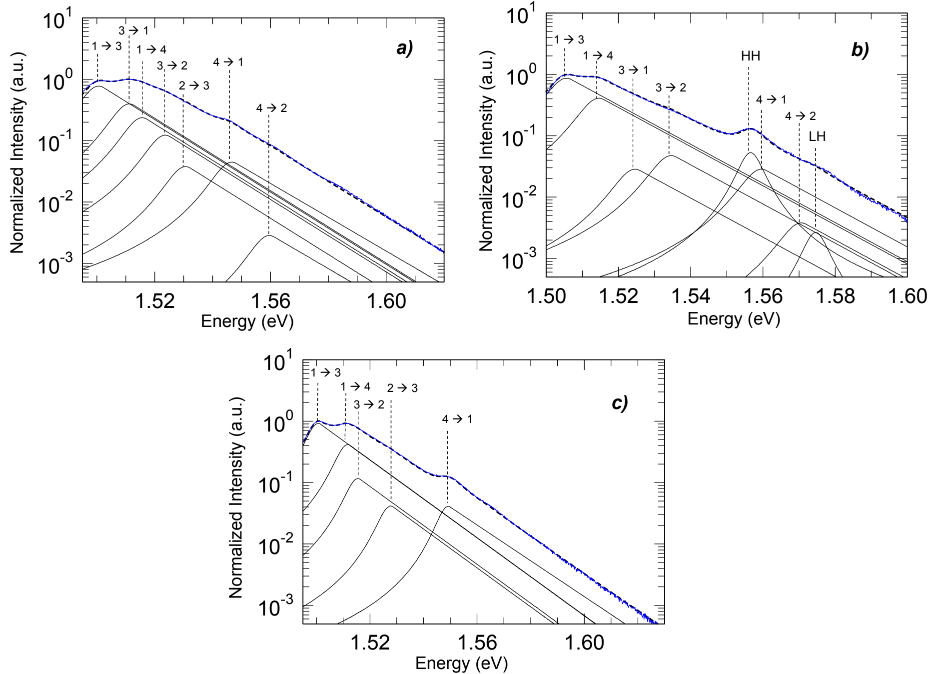

Fig. 4. (a-c): Representative photoluminescence spectra (blue lines) and best fit functions (dashed lines) of samples *a-c* under applied voltages per period / electric field of (64.3 mV / 17.8 kV/cm), (70.3 mV / 18.3 kV/cm), and (62.8 mV / 15.9 kV/cm), respectively. The heat sink temperature is $T_H = 50$ K. The calculated individual contributions associated with relevant j → k transitions are also shown.

#185600 - $15.00 USD Received 19 Feb 2013; revised 22 Mar 2013; accepted 22 Mar 2013; published 16 Apr 2013
(C) 2013 OSA

The main contributions to the PL spectra are due to transitions involving the conduction subbands j = 1 and j = 3, corresponding to the injection/extraction state and the higher laser level, respectively. This is qualitative in agreement with the expected higher populations of subbands j = 1 and j = 3, according to active region design [9]. Analogously, PL contributions involving the conduction subbands j = 2 and j = 4, are considerably weaker. This is quantitatively supported by the detailed PL analysis, as discussed later. Note that, in the sample *(b)* the contribution of transitions involving the conduction subband j = 2 is negligible. This is due to the small overlap integral of j = 2 with valence subbands (see Table 1) and to its expected low population.

In the PL spectra of sample *(b)* at threshold for current injection are clearly visible additional bands due to heavy-hole (HH) and light-hole (LH) excitons bound to the j = 4 subband (see Fig. 4(b)). The intensity of these excitonic contributions rapidly decrease at larger power densities and become negligible when $T_e > 160$. Similar excitonic transitions have been previously observed in bound-to-continuum THz QCLs [15]. In addition, the HH-LH splitting (~17 meV) is in agreement with the value expected for a GaAs quantum well ~12 nm wide, similar to the extension of the j = 4 wavefunction (~14 nm). These bands are fitted with Lorentzian functions with a half width at half maximum of ~1.8 meV, typical of excitonic peaks [24]. Similar structure are barely visible in sample *(c)* at threshold for current injection and not present in the PL spectra of sample *(a)* due to the higher T_e values that establish in this sample, as reported below.

Figure 5 shows the lattice and electronic subband temperatures as a function of the electrical power density, as extracted from the fitting procedure. The temperature values in the NDR regions are not reported because of the uncertainty in the electric field homogeneity. Note that below band alignment for carrier injection into level j = 4 we determine only the active region lattice temperature (see Figs. 1(a)-1(c)).

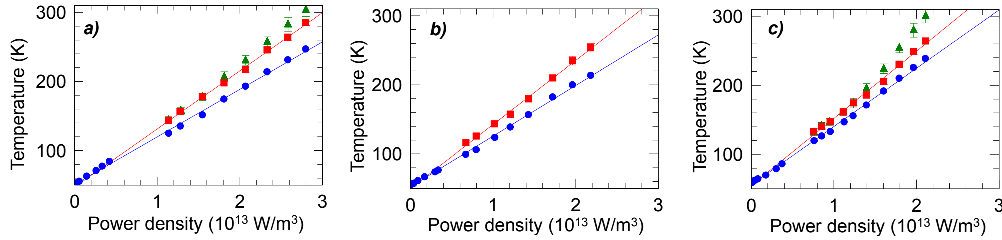

Fig. 5. Mean lattice temperature (●) and electronic temperatures $T_e^{1,2,3}$ (■) and T_e^4 (▲) in the active region of sample (*a*), (*b*) and (*c*) measured as a function of the electrical power at a heat sink temperature $T_H = 50$ K. Solid lines are linear fit to the data.

From the data of Fig. 5 we extracted the normalized thermal resistance [14] values $R_L^* = R_L \dfrac{A}{d}$ where $R_L = dT_L/dP$ is the device thermal resistance, and P is the electrical power. We found the values $R_L^* = 6.86$ K·cm/W for sample (*a*), $R_L^* = 7.11$ K·cm/W for sample (*b*), and $R_L^* = 8.42$ K·cm/W for sample *(c)*. These values are similar to those found in resonant-phonon active regions based on $GaAs/Al_{0.15}Ga_{0.85}As$ material system and double-metal contacts [13]. The larger R_L^* value measured for the sample (*c*) can be partly ascribed to the density of interfaces which is ~13% larger than samples (*a*), *(b)* [25].

As per the electronic subbands we found $T_e^j > T_H$. For all samples, subbands j = 1-3 share the same electronic temperatures that increase linearly with the electrical power density with slopes $R_e^* = 8.9$ K·cm/W, $R_e^* = 10.2$ K·cm/W and $R_e^* = 10.9$ K·cm/W for sample *(a)*, *(b)*, and *(c)*, respectively. Due to the presence of excitonic contributions at the PL spectra in the sample *(b),* we can extract the electronic temperature of the subband j = 4 only for high power densities (> 1.5×10^{13} W/m^3). In sample *(b)* the electronic temperatures of the injector state (j

#185600 - $15.00 USD Received 19 Feb 2013; revised 22 Mar 2013; accepted 22 Mar 2013; published 16 Apr 2013
(C) 2013 OSA

= 4) are identical to those of subbands j = 1-3, while in the samples *(a)* and *(c)*, T_e^4 show a larger increase with the electrical power density at power densities higher than 1.5 x 10^{13} W/m^3. At the largest values of the electrical power density in Fig. 5 the extra heating of the injector level T_e^4- $T_e^{1,2,3}$ is ~19 K in sample *(a)* and ~36 K in sample *(c)*, while the difference T_e^4 - T_L is ~57 K in sample *(a)*, ~44 K in sample *(b)*, and ~62 K in sample *(c)*. In analogy with previous reports [13, 26] the extra heating of the level j = 4, where electrons are resonantly injected from the ground level (j = 1') of the preceding stage, can be explained considering that while a comparable amount of power is distributed between the two subbands, the population n_4 is always at least one order of magnitude smaller than $n_{1'}$. It is worth noting that while in the conventional resonant phonon structures electrons are directly injected into the upper laser level, causing a large extra heating with respect to the lattice (ΔT ~70-110 K) or the ground level (ΔT ~100 K) [13, 26], in the present phonon-SA scheme both the laser levels j = 2,3 remains much colder (by a factor of 3-5) and share the same electronic temperature of the ground level (j = 1). From the measured R_e and R_L values we can extract the electron-lattice relaxation time $\tau_E = \frac{d}{A} N_e N K_B (R_e^* - R_L^*)$ where N_e is total number of electrons per stage and N is the number of stages. We found $\tau_E = 0.25\, ps$, $\tau_E = 0.41\, ps$ and $\tau_E = 0.26\, ps$ for sample *(a)*, *(b)* and *(c)*, respectively. These values are comparable with those found of resonant-phonon THz QCL [13] demonstrating that the electron-LO phonon scatterings, which couples the electron distribution to the lattice heat bath, are the dominant energy relaxation channel.

5. Relative electronic populations

From the best fit values of A_{jk} associated with transitions involving the same valence subband *k*, it is possible to extract the n_j / n_m population ratios. It is particularly interesting to examine the ratio n_2/n_1 as extracted from the PL bands associated with the 1⟶3 and 2⟶3 transitions bands (see Fig. 4 (c)). Figure 6 shows the ratio n_2/n_1 as a function of the electronic temperature for sample *(c)*. These values are shown together with n_2/n_1 values calculated assuming a thermal occupancy of the subbands j = 1 and j = 2 following the Maxwell-Boltzmann thermal distribution, $n_2 / n_1 = \exp(-E_{21} / K_B T_e^1)$, and using experimental electronic subband temperatures.

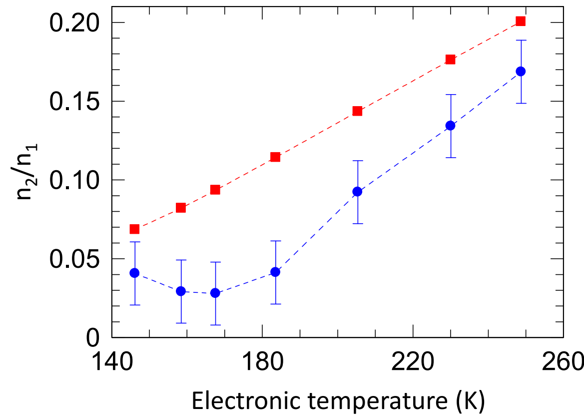

Fig. 6. Relative population n_2/n_1 between the lower laser level (j = 2) and the extractor level (j = 1) for sample *(c)* (●). Relative population n_2/n_1 calculated assuming a thermal populations of the subbands j = 1 and j = 2 for sample *(c)* (■). The dashed curves are guides for the eye.

#185600 - $15.00 USD Received 19 Feb 2013; revised 22 Mar 2013; accepted 22 Mar 2013; published 16 Apr 2013
(C) 2013 OSA

Our results show that the electronic population ratios n_2/n_1 remains below the value corresponding to the thermal occupancy due to the quasi-resonant optical phonon scattering. This process efficiently depopulates the lower laser level (j = 2) up to an electronic temperature T_e ~180 K. However, at larger T_e the ratio n_2/n_1 starts to increase with a rate comparable with the thermal activation one, thereby hindering the population inversion between the laser levels j = 3 and j = 2. Similar results are found for sample *(a)*.

6. Conclusion

We have measured and compared the electronic and lattice temperatures of three QCL active region structures based on the phonon-scattering assisted injection and extraction by means of microprobe band-to-band photoluminescence. A non-equilibrium hot electron distribution have been found. Differently from resonant phonon scheme where electrons are directly injected into the upper laser level, causing a large extra heating with respect to the lattice [13, 26], in the investigated phonon-SA injection and extraction scheme both laser levels remain much colder and share the same electronic temperature of the extractor level. The relative n_2/n_1 subbands electron population ratios shows an efficient lower laser level depletion at low electronic temperatures, whereas at temperatures larger than T_e ~180 K the ratio n_2/n_1 starts to increase with a rate comparable with the thermal activation one.

Acknowledgments

We gratefully acknowledge G. Palazzo for useful discussions on the spectral calibration analysis. This work is partially supported by Italian research projects: PON01_02238 and PON02_00675. The co-authors from Canada acknowledge D. Ban and H.C. Liu for their support and useful discussions on the design. M.S.V. acknowledges financial support of the Italian Ministry of Education, University, and Research (MIUR) through the program “FIRB-Futuro in Ricerca 2010” RBFR10LULP “Fundamental research on terahertz photonic devices”.

#185600 - $15.00 USD Received 19 Feb 2013; revised 22 Mar 2013; accepted 22 Mar 2013; published 16 Apr 2013

(C) 2013 OSA